Analysis of Liquid Flow through Ceramic Porous Media Used for Molten Metal Filtration

F.A. ACOSTA G., A.H. CASTILLEJOS E., J.M. ALMANZA R., and A. FLORES V.

A two-dimensional mathematical model has been developed to study fluid flow inside ceramic foam filters, used for molten metal filtration, as a function of their structural characteristics. The model is based on the selection of a unit cell, geometric model, formed by two interconnected half-pores. The good agreement between experimental and computed permeabilities showed that the unit cell model approximates very well the effect of filter structure on the flow conditions inside the filter. The validity of the model is supported by the fact that permeabilities are calculated from directly measured structural parameters, *i.e.*, without the introduction of any fitting variable, such as tortuosity. The laminar flow solutions for the Navier–Stokes equation, in steady state, were obtained numerically using the control-volume method. The boundary of the unit cell was represented through axisymmetrical, body-fitted coordinates to obtain a better representation of the complex pore shape. The generality of the model, to study fluid flow in reticulated media, was tested by comparing the computed specific permeabilities with values measured for ceramic foam filters and for the new ceramic filter of lost packed bed (CEFILPB). Such a comparison shows good agreement and discloses a fundamental property of the last kind of porous medium: the critical porosity. The model indicates how porosity and pore dimensions of reticulated filters may be tailored to meet specific fluid flow requirements.

I. INTRODUCTION

CERAMIC foam filters are playing an increasingly important role in the physical purification of metals, both in the ferrous and nonferrous industries. Certainly, the latter industry is the largest consumer of this filtering media, particularly the aluminum casting industry. Aubrey and Dore[1] reported that in 1992, eight million metric tons, equivalent to ~50 pct of all the aluminum produced in the world, was filtered using ceramic foam filters. The use of foam filters is also rapidly spreading toward filtration of high-temperature alloys. Sutton *et al.*[2] have reported results on the filtration of superalloys, and several articles present issues of plant and laboratory tests in the filtration of cast irons and steels.[3–6] Recently, Garing and Cummings[6] announced the successful filtration of carbon and alloy steels using ceramic foam filters, in the tundish of a four-strand bloom caster. The results from these works look so promising that one could expect that filtration may soon become a clean steel-making practice.

The wide acceptance of ceramic foam filters is based on their structural properties, which allow the filter, among other things, to have a low flow resistance and a high filtration efficiency. The webs (ceramic elements of the structure) of these filters create a tortuous path for the fluid to flow through favoring the probability of inclusion contact with the internal surfaces of the filter; *i.e.*, for inclusions much smaller than the pore size, the foam filters provide deep bed filtration. The filtration efficiency of foam filters is closely related to the fluid flow conditions through the porous medium.[7] Fluid flow plays an important role in transporting inclusions to the filter wall where they can attach, but also, it can be responsible for dragging out the captured inclusions. Several publications indicate that filtration efficiency decreases with increasing superficial melt velocity.[1,7,8] Aubrey and Dore[1] found that foam filters, having a pore size of 30 ppi (pores per inch) and a thickness of 2 inches, worked efficiently in the filtration of aluminum at mass fluxes between 70 and 200 g/cm^2 min, *i.e.*, for aluminum melt superficial velocities between 0.5 and 1.5 cm/s. They observed that capture efficiency decreased dramatically above that range.

From the previous arguments, it is clear that it is desirable to be able to predict the flow rate obtainable under a given pressure drop or to be able to predict the pressure drop necessary to achieve a specific flow rate. In fluid mechanics of granular porous media, the relationship between these quantities is represented by the Ergun equation,

$$|\nabla P| = (a_1 + a_2 Q)Q \qquad [1]$$

where a_1 ($=\mu/KA$) and a_2 are coefficients that account for laminar and turbulent effects, respectively. The Darcy viscous specific permeability, K, can be determined either experimentally by measuring pressure gradient *vs* flow rate or theoretically from packing structure properties. However, for ceramic foam structures, there is not a reported relationship between structure properties and specific permeability. Under these circumstances, ceramic foam filters manufacturers have generated experimental data showing indirectly, the permeability of their products as plots of percent of original flow rate *vs* filter area/choke area ratio, for filters of different pore sizes.[3] The metal flow rate is held at a value close to the no-filter situation by using filters with an area several times larger than the choke area of the gating system. Proper filter sizing is also important to

F.A. ACOSTA G. and A. FLORES V., Assistant Professors, A.H. CASTILLEJOS E., Associate Professor, and J.M. ALMANZA R., Research Assistant, are with the Investigation Center and Advanced Studies of the IPN, CINVESTAV-Unidad Saltillo, Saltillo 25000, Coah, Mexico.

Manuscript submitted November 9, 1993.

avoid premature filter blockage by inclusions.[3,6] Sutton *et al.*[2] have indicated that the resistance of a given filter to metal flow can be reduced considerably by increasing the pore size and porosity and by decreasing the web thickness, but this is achieved at the expense of weakening the filter structure. The authors indicate that to explain differences in the permeability of filters is necessary to consider the complex effects that pore shape and size, porosity, and webs structure have on it.

Filter permeability also plays a role in promoting flow regulation downstream the filter, *i.e.*, the achievement of laminar flow conditions under specific flow rates.[9] Flow regulation acts in preventing the penetration of vorticity in the inlet flow, in reducing turbulent entrainment of foreign materials, and in limiting metal reoxidation and mold erosion.

The complexity of most porous media makes impossible the exact description of the solid boundaries that are determinant for the characteristics of fluid flow inside the filters. Therefore, before pursuing a microscopic model to determine filtration efficiency, it is necessary to obtain a geometric model that resembles the pore structure and also approximates its overall effect to flow. Being that the specific permeability is an intrinsic property of the structure of porous media, it has been used by Payatakes and co-workers[10,11,12] to validate geometric models of granular porous media and fluid flow behavior within them. Payatakes *et al.*[10] developed a model for isotropic monosized granular porous media based on a single unit cell. The model considered the convergent-divergent character of the flow ducts and the random dimensions of pores and constrictions and was used[11] to carry out trajectory calculations of particles in deep bed filtration. In a subsequent work,[12] the unit cell model was further improved by considering the random orientation of pores and constrictions. The authors calculated the flow field within the unit cell and from it the permeability, and they found an excellent agreement between experimental and calculated permeability values. In a different approach to the unit cell model, Tian and Guthrie[13] studied fluid flow in porous media by representing the ceramic web structure of foam filters by a number of orderly placed cylindrical obstacles. The porosity of the porous media was prescribed by varying the number density of obstacles. This geometric model was used to calculate the fluid flow field within the filter and from it the permeability. Apparently, the fitting of predicted with measured permeabilities was used as the criterion for the placement and sizing of the obstacles representing the filter walls. Gauckler *et al.*[14] used the method of Payatakes *et al.*[11] to investigate the filtration behavior of ceramic foam filters to purify molten aluminum. However, the investigators did not give details on the flow patterns used in their filtration efficiency calculations. Engh *et al.*[15] developed a theory to study the deposition of solid particles on single spherical or nonspherical collectors and extended it to determine collection efficiencies for packed beds of spheres. The effect of the roughness of the collector surface on collision efficiency has been discussed in the literature.[16,17]

The results reported in this study represent the start of a long-range investigation whose objective is the development of a comprehensive theory of deep bed liquid filtration with foam filters. Such a theory requires a geometric model that resembles the pore structure of the filter media and also approximates its overall effect to flow. This article addresses the problem of creeping Newtonian fluid motion in ceramic foam filters and in ceramic filter of lost packed bed (CEFILPB)[8,18,19] or pore-formed ceramic filters.[20,21,22] The approach is based on the selection of a unit cell formed by two interconnected half-pores. The unit cell is considered a section of a periodically constricted tube with average dimensions and orientation. These geometric parameters are obtained from the measured distributions of pore and window (interconnecting openings between pores) diameters and by considering the random orientation of the pores. For accurate modeling of the fluid flow within the complex geometry of the unit cell, a body-fitted coordinate system was employed. The governing Navier–Stokes equation was solved numerically using a control-volume technique. This work generalizes the ideas of Payatakes *et al.* by introducing a relationship between the porosity, the average pore coordination number (number of windows in a pore or number of closest neighboring pores to a given one), and the window-to-pore diameter ratio, all of which have an effect on the motion of fluid through porous media. To validate the proposed model, the permeabilities of foam and CEFILPB filters were measured and compared with the corresponding calculated values. A good agreement was found, and the model helped to disclose the existence of a critical porosity in pore former filters. The modeling of the pore space and of the fluid flow within it forms the basis for the study of deep bed filtration, which is presently pursued.

II. FORMULATION OF THE PROBLEM

A. *System Considered*

The fluid flow and permeabilities of the ceramic porous bodies shown in Figures 1(a) and (b) have been investigated. These are filters of high porosity (>70 pct). The fabrication process for the foam filters involves coating a polyurethane foam with a ceramic slurry that is let to dry for later burn off of the polymer. The process results in a positive replica of the foam where the pores are surrounded by interconnected empty strands of ceramic. On the other hand, the CEFILPB, or pore former filters, are obtained by saturating the interstitial spaces of a packed bed of particles with a ceramic slurry. After the slurry has dried out and the ceramic structure has achieved enough green strength, the particles are leached out. This is the reason for the name lost packed bed filters. The process leads to a ceramic structure that corresponds to the negative of the packed bed structure. The nature and flexibility of this process allow it (a) to obtain compact ceramic walls; (b) to control porosity, pore size, and pore shape; (c) to avoid flow channeling; and (d) to have small interconnecting windows between the pores. The control on the dimensions of the flow passages is very useful for tailoring permeabilities.

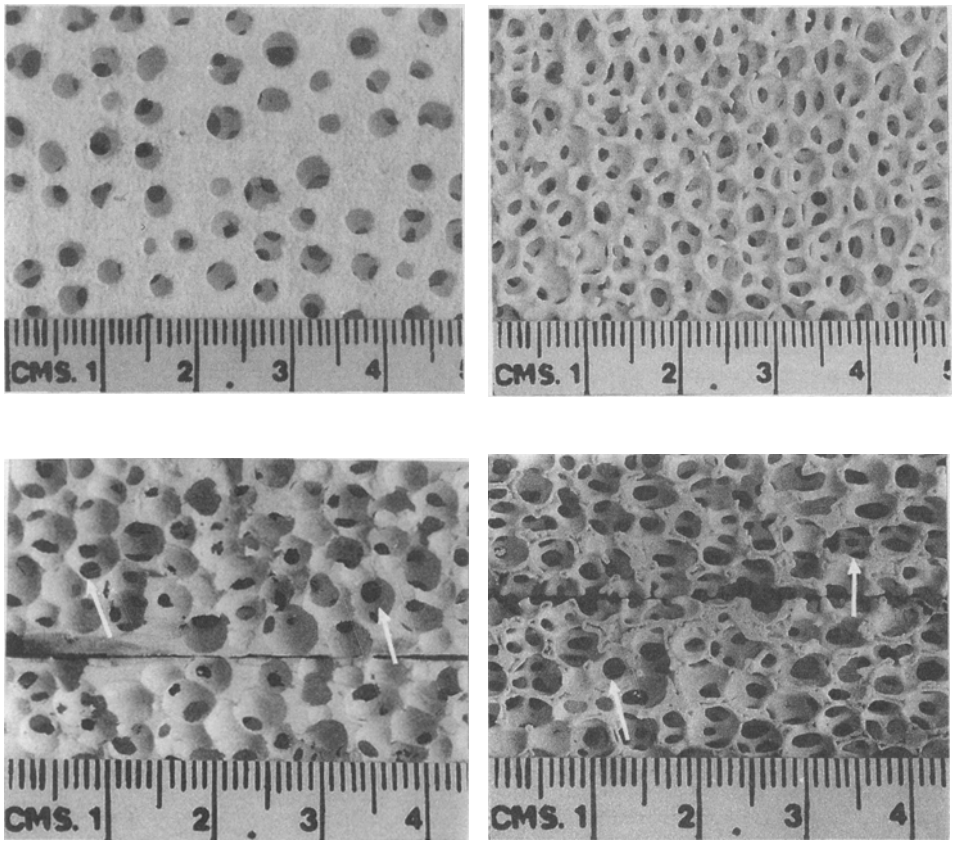

(*a*) (*b*)

Fig. 1—Photographs of views perpendicular and parallel to the direction of flow of (*a*) CEFILPB and (*b*) foam filters.

B. *Experimental Work*

The experimental work consisted of measuring filter permeabilities to validate the calculations and determining pore and window sizes and porosity, which are the parameters needed by the mathematical model.

The specific permeabilities were measured in filters of a 50-mm diameter and 20-mm thick, using water flowing in a closed loop, as that shown in Figure 2. Pressure drops for different water flow rates were measured twice, once for each filter face oriented upstream. Figure 3 shows plots of macroscopic pressure gradient *vs* water flow rate obtained for a CEFILPB and a foam filter. From this figure, it is seen that the measured

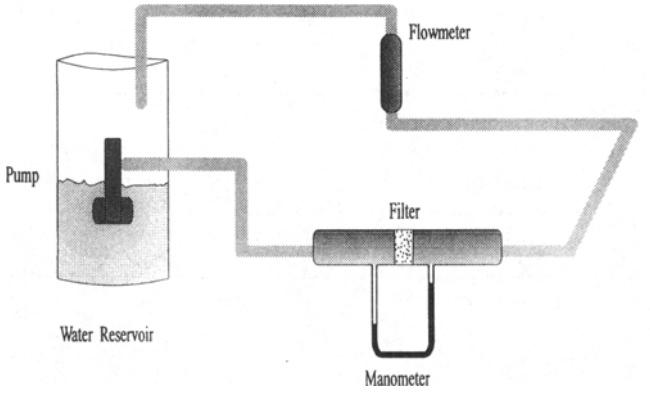

Fig. 2—Scheme of the closed water loop used for measuring permeability of filters.

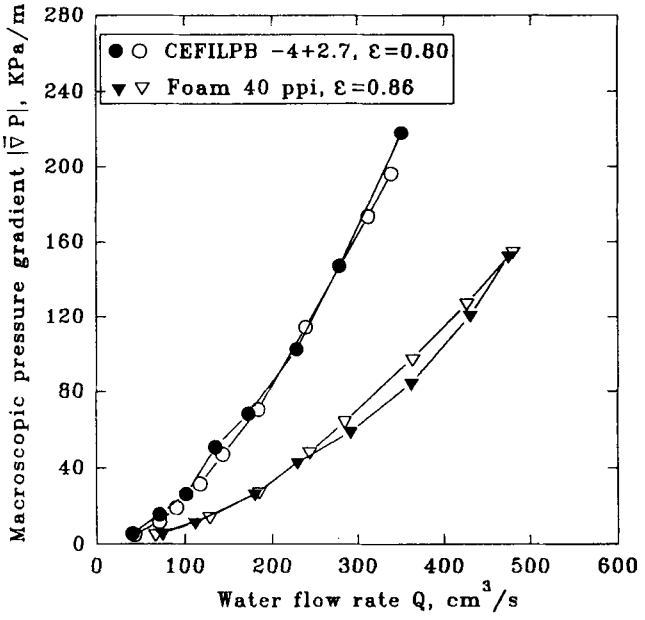

Fig. 3—Plots of measured pressure gradient as a function of water flow rate. Two flow directions were tested for every filter as indicated by the empty and full symbols.

pressure gradients are essentially independent of the surface facing upstream, indicating that the filters are isotropic. Figure 3 also indicates that, as expected from Ergun's equation for porous media (Eq. (1)), the pressure gradient through the filter follows a parabolic relationship with the flow rate. The specific permeability, K, was determined from the experimental results by fitting a parabola to them and computing the slope of the $|\nabla P|$ *vs* Q curve at zero flow rate, *i.e.*, laminar flow conditions. Table I presents the mean specific permeabilities measured on particular foam and CEFILPB filters of different nominal pore sizes. For ceramic foam filters, the nominal pore size is given in pores per inch (ppi), while for CEFILPB filters it is given in terms of the diameter of the pore former. Table II reports additional foam filter permeabilities measured in this work and in those of Tian and Guthrie[13] and Sane *et al.*[20] From the table, it is seen that permeability may vary appreciably for filters of the same nominal pore size and that porosity alone does not explain the observed changes in permeability values. As shown later in this section, the cell and window size distributions also play a role in determining the permeability of the porous medium, *i.e.*, fluid flow behavior.

The pore and window size distributions were obtained optically with the help of an image analysis system using an intercept length method. For the determination, the filters were impregnated with a transparent resin before cutting them along a plane parallel to the direction of flow; the resin avoided breakage of the ceramic walls. The Spektor's method was utilized to determine pore diameter distribution from measured chord lengths.[23] Since the pores are slightly ellipsoidal, the chords were measured, both, in the parallel and perpendicular directions to the flow, and the mean pore size was defined as the average of the two mean diameters. The average pore and window sizes for particular filters of different nominal size are given in Table I. The window diameters were determined by measuring the diameters of complete windows located parallel to the cut plane and just below it, examples of this type of window are indicated by the arrows appearing in Figure 1. A typical window size distribution for a foam filter is shown in Figure 4. The window size distributions allowed one to obtain the statistical quantities required by the model, the third and fifth momenta of the window size.

The pore porosity, ε, was measured according to the specification ASTM C20-87 applicable to ceramic refractories. In this method, the porosity is obtained by dividing the weight of water retained in the macropores of the filter by the weight of water that occupies a volume equivalent to that of the whole filter. The porosity values for randomly chosen samples of CEFILPB and foam filters are presented in Table I. Figure 5 shows these porosity values plotted as a function of $\langle d_w \rangle / \langle d_c \rangle$. The black dots, corresponding to pore former filters, show that porosity increases with the increase in diameter ratio; this relationship is somewhat irregular in the case of foam filters.

C. *Mathematical Formulation*

1. *Representation of the filter structure*

From the photographs appearing in Figure 1, it is clear that the complexity of the porous structure would make it quite difficult to specify the location of the pore walls and, therefore, of the boundary domain. Furthermore, if the entire filter was used as the calculation domain, the required computer storage and computer time would be truly excessive. A useful simplification arises by assuming that the fluid flow is fully developed, such that the velocity field repeats itself pore after pore. However,

Table I. Experimentally Determined Properties of Ceramic Foam and CEFILPB Filters

Nominal Pore Size	K (KDarcy)	$\langle d_c \rangle$ (mm)	$\langle d_w \rangle$ (mm)	$\langle d_w \rangle / \langle d_c \rangle$	ε
10 ppi	43.0	3.85	1.69	0.44	0.8
15 ppi	45.3	3.15	1.13	0.36	0.89
20 ppi	38.9	2.55	1.15	0.45	0.82
30 ppi	16.0	2.06	0.93	0.45	0.88
40 ppi	14.4	1.37	0.69	0.5	0.86
50 ppi	7.8	0.98	0.53	0.54	0.88
−2.7 + 2 mm	4.8	1.75	0.71	0.4	0.79
−4 + 2.7 mm	6.0	1.93	0.83	0.43	0.8
−6.3 + 4 mm	19.3	3.41	1.94	0.57	0.85

Table II. Typical Porosities and Specific Permeabilities of Ceramic Foam Filters, Reported by Different Authors

Nominal Pore Size	ε[16]	K (KDarcy)[16]	ε (Present Work)	K (KDarcy) (Present Work)	ε[12]	K (KDarcy)[12]
30 ppi	0.78	6.96	0.87	14.3	0.85	18
	0.87	15.02	0.88	16.0	0.89	40
45 ppi	0.81	3.75	—	—	0.8	10
	0.88	9.59	—	—	—	—
40 ppi	—	—	0.86	14.4	—	—
50 ppi	—	—	0.88	7.8	—	—

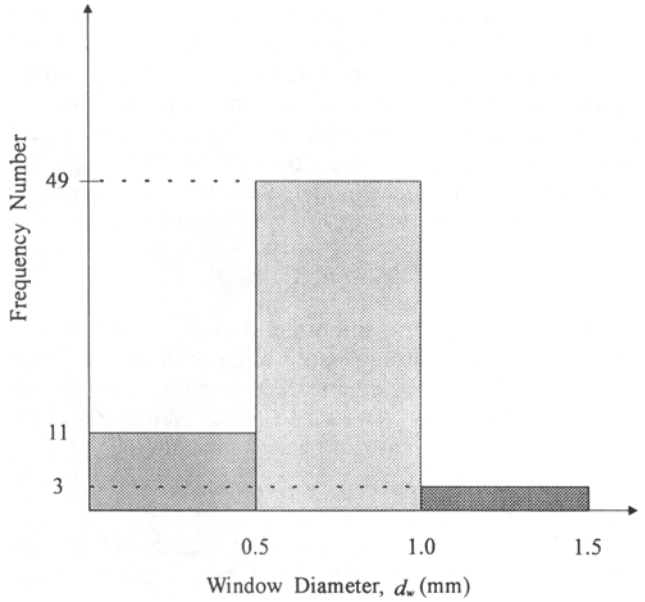

Fig. 4—Histogram showing typical window diameter distribution of a foam filter.

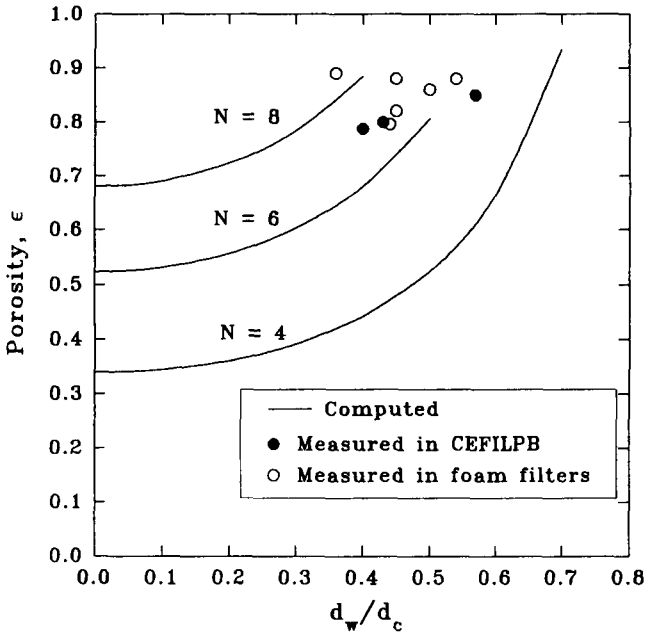

Fig. 5—Computed and experimentally determined porosities as a function of window-to-cell diameter ratio, for sphere arrangements with different coordination numbers.

this task needs the adequate selection of a geometrical pore module that reflects the pore coordination number, the random distribution of pore and window diameters, and orientation and curvature of the pore walls.

The coordination number can be estimated from visual inspection of sectioned filters. However, a more reliable method can be obtained by considering different packing modes of the pore former and recognizing that the packing fraction, *i.e.*, porosity, is related to the ratio d_w/d_c and to the coordination number, N. As mentioned in Section A, CEFILPB filters are made by impregnating a packed bed of spheres with a ceramic slurry. When these particles are leached out, the remaining ceramic body has a porosity equal to the particle packing fraction of the original bed. From geometry, the packing fraction of the arrays of spheres shown in Figure 6, for coordination numbers 4, 6, and 8, are 0.34, 0.52, and 0.68, respectively. In these unit lattices, rigid spheres are in mutual contact in just one point; *i.e.*, the resulting adjacent pores would have a window diameter equal to zero. However, CEFILPB filters are formed by well-interconnected pores that are produced from spheres being in mutual contact over a finite area. To determine the dependence of the window size on the packing fraction, let us consider the overlapping between two neighbor pore former spheres when the distance between their centers decreases, from a distance d_c, the pore diameter, to a distance equal to $2x_0$, the distance between the centers of interconnected pores. The size of the window appearing depends on the degree of overlapping (Appendix). The relationship of the porosity with N and d_w/d_c can be obtained considering the following definition:

$$\varepsilon = \frac{V_s}{V_t} \qquad [2]$$

where V_s is the volume occupied by the spheres contained within a unit lattice of volume V_t and side length

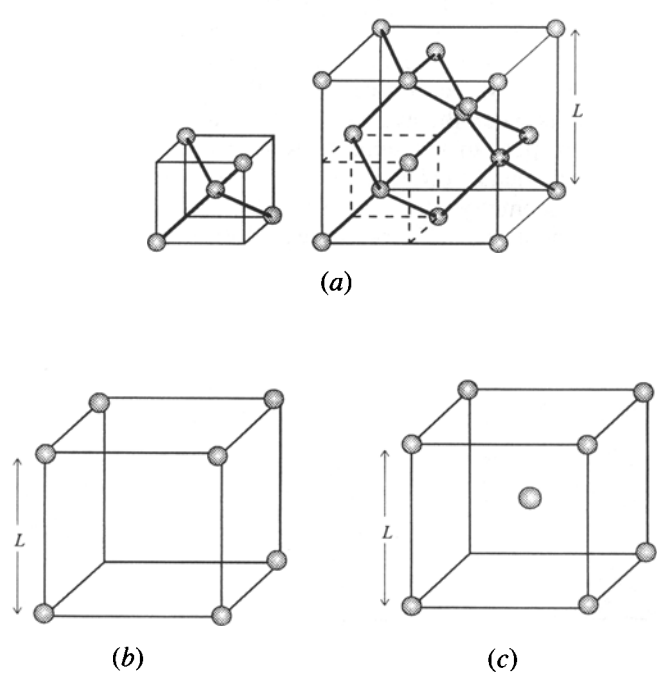

Fig. 6—Unit cell lattices showing spheres with different coordination numbers: (*a*) diamond cubic lattice, $N = 4$; (*b*) cubic lattice, $N = 6$; (*c*) body-centered cubic lattice, $N = 8$.

L (Figure 6). Table III shows the parameters used to calculate the porosity for lattice arrangements of different coordination numbers. For the calculations, it is assumed that, despite their overlapping, the volume of the spheres remain constant. Figure 5 shows the calculated filter porosity as a function of d_w/d_c for three coordination numbers. The figure indicates that a larger porosity, *i.e.*, a closer packing of the pore former, results

Table III. Lattice Parameters Used to Calculate Filter Porosities

Lattice Denomination	Coordination Number N	Number of Spheres per Lattice	Cube Side Length L
Diamond cubic	4	8	$4.62x_0$
Cubic	6	1	$2x_0$
Body-centered cubic	8	2	$2.31x_0$

in higher values of d_w/d_c for a given coordination number. A comparison of the experimental values of ε *vs* d_w/d_c with the calculated curves indicates that the coordination number for both foam and CEFILPB filters is close to six. Visual inspection of the filters structure reveals a similar value.

Figure 7 displays schematically a single pore having windows centered on the axes A, B, and C, which corresponds to a coordination number of six. In the figure, the X-axis indicates the main flow direction, and θ represents the random angle between the pore axis, C, and the X-axis. Due to the complexity of the filter structures, the pores are randomly oriented; *i.e.*, θ can take values in the range from 0 to $\pi/2$. When the angle θ has a value equal to zero, the whole flow occurs through the windows located on the C-axis. This axis remains the preferred flow direction for angles $0 \leq \theta < \alpha$. The angle α occurs when the axes A, B, and C are equally inclined with respect to the main flow direction, and the fluid flow is equally probable along any of these three axes. From geometry, it is found that for a pore coordination number of six, $\alpha = 54.74$ deg. With this consideration in mind, we can postulate that the fluid flow in the macroscopic transport direction can be represented by the flow occurring through a unit cell having only one

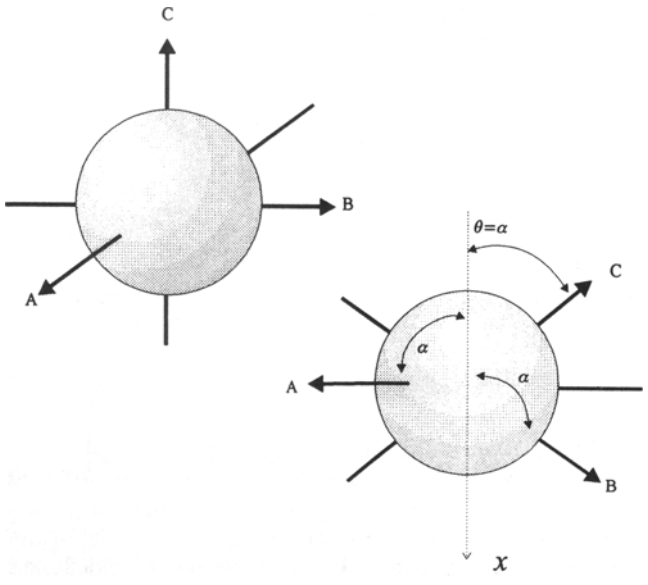

Fig. 7—Schematic of a pore with a coordination number of six, illustrating the random nature of pore orientation with respect to the main flow direction.

inlet and one outlet and which incorporates the flow constriction represented by the window. Thus, the unit cell selected to represent foam and CEFILPB filters is built by two half-pores, as it is shown in Figure 8. The unit cell has an inlet and an outlet having a diameter equal to the pore diameter and a constriction surface with a diameter equal to the window diameter. The length of the unit cell can be expressed as (Appendix)

$$L = 2x_0 = d_w(C_1^2 - 1)^{1/2} \qquad [3]$$

where $C_1 = d_c/d_w$. It is important to mention that d_c, d_w, and x_0 are related through only one constant, C_1, since the pore geometry is spherical. Nonspherical pores require more than one constant to relate their internal dimensions, as is the case in packed bed filters.[10,11,12]

2. *Assumptions, governing equations, and boundary conditions*

For the purpose of calculations, it is assumed that the unit cell for foam and CEFILPB filters is the same despite the differences in their method of fabrication. Additionally, the following assumptions are made: (1) the fluid flow through any unit cell is fully developed; *i.e.*, there is a common pressure drop across any unit cell within the filter; (2) the fluid flow is laminar; (3) the fluid flow is axisymmetrical; this assumption is acceptable because the fluid moves predominantly in the main flow direction as pointed out previously; and (4) the fluid flow through the unit cell occurs under steady-state conditions.

The governing differential equations for the velocity and pressure fields within the unit cell are given by the continuity and Navier–Stokes equations, which are written as

$$\nabla \cdot \mathbf{u} = 0 \qquad [4]$$

$$-\nabla p - \nabla(\rho \mathbf{u}:\mathbf{u}) + \mu \nabla^2 \mathbf{u} + \rho \mathbf{g} = \mathbf{0} \qquad [5]$$

The boundary conditions are specified as follows:

1. *Axis of the unit cell*: zero flux conditions are imposed as a result of axisymmetry

$$\frac{\partial u_x}{\partial r} = 0 \qquad u_r = 0 \qquad [6]$$

2. *Unit cell walls*: nonslip and impermeable conditions are imposed; *i.e.*, flow velocities tangential and normal to the wall are zero.

3. *Inlet and outlet*: across any given unit cell, there is a prescribed common pressure drop, ΔP_{UC}, defined as

$$-\Delta P_{UC} = |\nabla P| 2x_0 \cos\theta \qquad [7]$$

Where $|\nabla P|$ is the magnitude of the macroscopic pressure gradient acting on the filter and x_0 and θ are random variables, which meanings have previously been given (Section C–1).

3. *Derivation of the mathematical expression for the permeability*

In order to validate the fluid flow calculations under laminar flow conditions, an expression for the specific permeability, K, as a function of the geometry of the

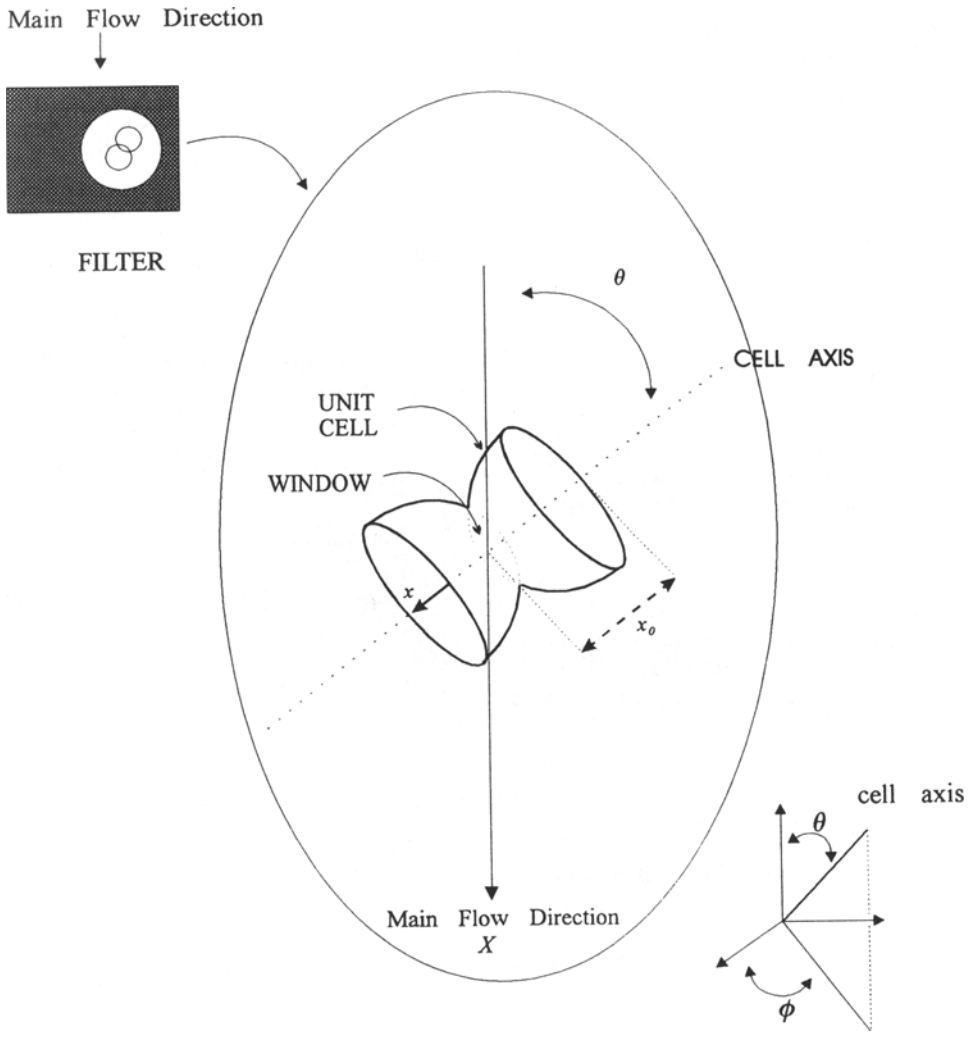

Fig. 8—Selected unit cell for CEFILPB and foam filters, showing the orientation angles θ and ϕ and the characteristic dimensions d_w, d_c, and $2x_0$.

porous structure has to be obtained. From Darcy's law, it is known that

$$u_s = K\frac{|\nabla P|}{\mu} \qquad [8]$$

and from continuity, the superficial velocity, u_s, is

$$u_s = \langle u_X \rangle \varepsilon \qquad [9]$$

where $\langle u_x \rangle$ is the mean fluid velocity, within the filter, in the direction of the main flow, *i.e.*, X-direction. This velocity can be computed from the X-momentum of the fluid as it passes the filter,

$$M_X = \rho \varepsilon V_m \langle u_X \rangle \qquad [10]$$

which in turn, it is defined as

$$M_X = V_m N_p \int_E m_X(d_w, \theta) dE \qquad [11]$$

where V_m is the volume of the porous medium, N_p is the number of pores per unit volume, m_x is the X-momentum in a unit cell, d_w is the random window diameter, and dE is the joint probability density function of the random variables d_w, θ, and ϕ that characterize the unit cell,

$$dE(d_w, \theta, \phi) = \frac{\sin\theta}{2\pi(1 - \cos\alpha)} d\phi d\theta dd_w \qquad [12]$$

The X-fluid momentum in the unit cell is calculated from the fluid flow field according to the following expression:

$$m_X = \rho \int_{V_{UC}} [u_x]_X dv \qquad [13]$$

where $[u_x]_X$ is the projection of the u_x velocity in the X-direction. For the purpose of this work, Eq. [13] can be written as

$$m_X = \rho \int_0^{2x_0} \left\{ \int_A [u_x]_X dA \right\} dx \qquad [14]$$

where A is the cross-sectional area of the pore at any given x position. The quantity inside the key bracket is the voluminic flow rate in the X-direction, q_{UC}, which is

related to the voluminic flow rate through the cell, Q_{UC}, according to the following expression:

$$q_{UC} = Q_{UC} \cos \theta \quad [15]$$

therefore,

$$m_X = \rho \int_0^{2x_0} Q_{UC} \cos \theta dx \quad [16]$$

and since Q_{UC} is independent of x, then

$$m_X = \rho 2x_0 Q_{UC} \cos \theta \quad [17]$$

The term Q_{UC} can be calculated from the velocity field obtained by solving Eqs. [4] and [5]. For convenience, the flow rate is written in terms of the mean flow velocity and cross-sectional area of the window, u_w and A_w, respectively,

$$Q_{UC} = u_w A_w \quad [18]$$

An expression for u_w in terms of the structural parameters of the unit cell can be obtained introducing the following definitions: (a) the dimensionless pressure drop across a unit cell,

$$\Delta P^*_{UC} = \frac{\Delta P_{UC}}{\rho u_w^2} \quad [19]$$

and (b) the dimensionless pressure drop corresponding to a Reynolds number equal to one,

$$\Delta P^*_1 = N_{Re} \Delta P^*_{UC} \quad [20]$$

The Reynolds number has been defined as $N_{Re} = 2x_0 u_w \rho / \mu$. From Eqs. [7], [19], and [20] and from the Reynolds number definition, the following expression is obtained:

$$u_w = \frac{(2x_0)^2 |\nabla P| \cos \theta}{\mu(-\Delta P^*_1)} \quad [21]$$

then,

$$m_X = \frac{\rho(2x_0)^3 |\nabla P| \cos^2 \theta A_w}{\mu(-\Delta P^*_1)} \quad [22]$$

Substitution of Eqs. [22] and [3] into Eq. [11] results in the following expression for the total X-momentum of the fluid within the filter:

$$M_X = \frac{V_m N_p \rho |\nabla P| (C_1^2 - 1)^{3/2} \pi}{4\mu(-\Delta P^*_1)} \int_E d_w^5 \cos^2 \theta \, dE \quad [23]$$

Evaluating the integral over the limits $\phi \in \{0, 2\pi\}$, $\theta \in \{0, \alpha\}$, and $d_w \in \{d_{w,min}, d_{w,max}\}$, the following expression is obtained:

$$\int_E d_w^5 \cos^2 \theta \, dE = \frac{(1 + \cos \alpha + \cos^2 \alpha)}{3} \langle d_w^5 \rangle \quad [24]$$

where $\langle d_w^5 \rangle$ is the fifth momentum of the window diameter distribution and is expressed as

$$\langle d_w^5 \rangle = \int_{d_{w,min}}^{d_{w,max}} d_w^5 f_{d_w} dd_w \quad [25]$$

the number of pores per unit volume is given as

$$N_p = \frac{\varepsilon}{\langle V_{UC} \rangle} \quad [26]$$

where the average unit cell volume is

$$\langle V_{UC} \rangle = F(C_1) \langle d_w^3 \rangle \quad [27]$$

$\langle d_w^3 \rangle$ is the third momentum of the window diameter, defined as

$$\langle d_w^3 \rangle \int_{d_{w,min}}^{d_{w,max}} d_w^3 f_{d_w} dd_w \quad [28]$$

and the function $F(C_1)$ (Appendix) is

$$F(C_1) = \frac{\pi}{8} \left[2C_1^2 (C_1^2 - 1)^{1/2} - \frac{2}{3} (C_1^2 - 1)^{3/2} \right] \quad [29]$$

From Eqs. [26] and [27], the number of pores per unit volume of filter can be rewritten as

$$N_p = \frac{\varepsilon}{F(C_1) \langle d_w^3 \rangle} \quad [30]$$

Finally, substitution of the Eqs. [9], [10], [23], [24], and [30] into Eq. [8] results in the following expression for the specific permeability, K,

$$K = G(C_1) H(\alpha) \frac{\langle d_w^5 \rangle \varepsilon}{\langle d_w^3 \rangle (-\Delta P^*_1)} \quad [31]$$

where

$$G(C_1) = \frac{C_1^2 - 1}{2C_1^2 + 1} \quad [32]$$

and

$$H(\alpha) = 1 + \cos \alpha + \cos^2 \alpha \quad [33]$$

The importance of Eq. [31] is that the specific permeability can be calculated in terms of easily measurable parameters, *i.e.*, the porosity, ε; the third and fifth momenta of the window diameter, $\langle d_w^3 \rangle$ and $\langle d_w^5 \rangle$; the ratio of mean pore diameter to mean window diameter, C_1; the limit angle α, which is a function of the coordination number; and the computed dimensionless pressure drop, ΔP^*_1.

III. SOLUTION PROCEDURE

The differential equations of mass and momentum conservation were solved using the control volume method implemented in the PHOENICS code. An accurate representation of the unit cell surface and therefore a reliable prescription of the boundary conditions at this surface was achieved using the body-fitted coordinate system capability included in PHOENICS. Poisson's equation was solved to transform the coordinate system from the physical plane to a computational

plane and generate a mesh with improved grid orthogonality. The method of orthogonal attraction over the wall boundary was chosen, specifying that the grid lines normal to that boundary are orthogonal to it. Two nonuniform grids, (30 × 10) and (48 × 24), were used in the computations to assess the grid size sensitivity. Only minor differences in the results obtained from both meshes were observed, and therefore, most of the calculations were done with the coarser grid shown in Figure 9. This mesh allowed time savings without sacrificing accuracy. Convergence was based on the following criterion:

$$\text{Max}(|R_v^{k+1} - R_v^k|/|R_v^{k+1}|) \leq 1 \times 10^{-4} \qquad [34]$$

where R_v^k is the local value of the v variable (pressure or velocity) in the k iteration. It was found that the convergence of the numerical solution, in the tiny flow domain under consideration, was favored by the use of microns as the length dimension.

The procedure for computing the dimensionless pressure drop, ΔP_1^*, was to solve Eqs. [4] and [5] for different values of ΔP_{UC}, *i.e.*, different boundary values at the inlet and outlet, until the flow velocity profile at the window resulted in a mean average velocity such that the Reynolds number was equal to one.

IV. RESULTS AND DISCUSSION

Figures 10(a) and (b) show typical fluid velocity and pressure fields corresponding to an $N_{Re} = 1$, respectively. The fields are computed for water flowing inside the unit cell of a filter with a $d_w/d_c = 0.4$ and a length $L = 1.6$ mm; these dimensions belong to the CEFILPB filter with a nominal size of $-2.7 + 2$ mm reported in Table I. It should be made clear that the same calculations would be valid for a foam filter with identical values of the structural parameters d_w/d_c and L. Although the unit cell was derived from analyzing the pore former filter structure, the permeability calculations given below demonstrate that it is also valid for representing the pore structure in foam filters. Figure 10(a) shows that for laminar flow conditions, there is not recirculatory flow; also, there is a strong variation of the velocity along the axial direction, and large quasi-stagnant zones occur close to the pore wall. Figure 10(b) indicates that the pressure drop, through the unit cell, happens mainly in the vicinity of the window.

The dimensionless pressure drop, ΔP_1^*, through a unit cell was determined considering the flow of aluminum, water, and air through the unit cell. The physical properties of the three fluids are given in Table IV. It was found that the values of dimensionless pressure drop for the three cases did not differ by more than 5 pct. This behavior indicates that ΔP_1^* depends exclusively on pore structure and not on fluid properties. Thus, from Eq. [31], it is clear that also the specific permeability, K, is only a function of the pore structure. These results are in agreement with that found in the literature for granular porous media.[24] Table V reports the dimensionless pressure drop for filters of different nominal pore size. The computation of the pressure drop was also

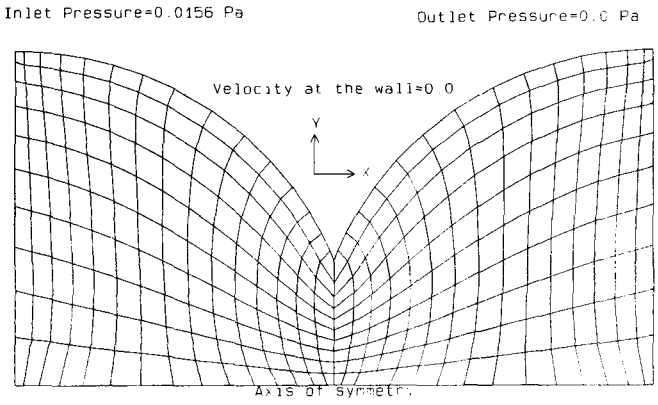

Fig. 9—Schematic of axisymmetric unit cell system, illustrating the 30 × 10 body-fitted grid and the boundary conditions.

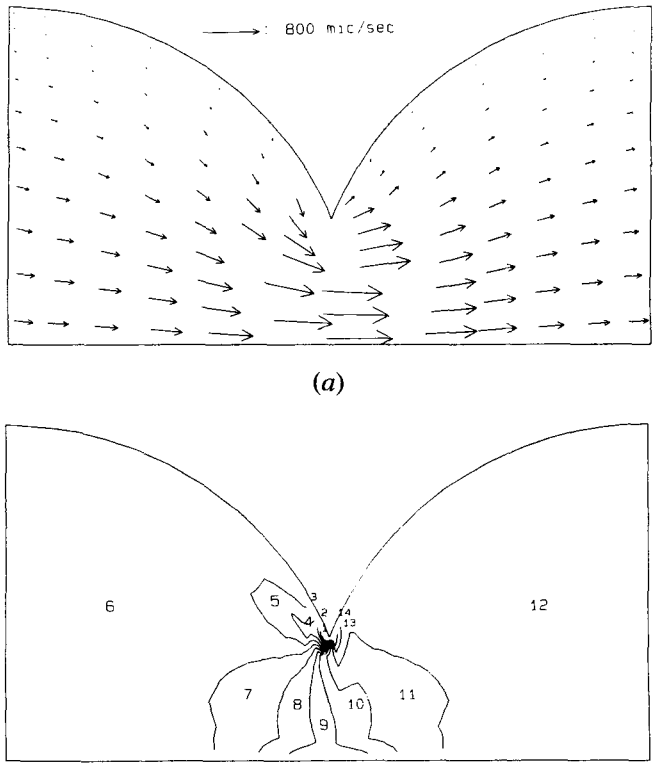

Fig. 10—Predicted (*a*) mean velocity field and (*b*) pressure distribution for water flowing, at a $N_{Re} = 1$, through a unit cell with a ratio $d_w/d_c = 0.4$ and a length $L = 1.6$ mm. The numbers on the contours indicate relative pressure uniformly spaced from 3×10^{-2} to -6.6×10^{-3} Pa.

Table IV. Fluid Physical Properties Used in Permeability Calculations

Fluid	Density ρ (Kg/μm^3)	Kinematic Viscosity ν (μm^2/s)
Air	1.200×10^{-18}	1.50×10^{7}
Water	9.982×10^{-16}	1.01×10^{6}
Aluminum	2.300×10^{-15}	5.17×10^{5}

Table V. Parameters Involved in the Model to Compute Specific Permeability, Equation [32], $H(\alpha = 54.74\ \text{Deg}) = 1.91055$

Nominal Pore Size	$G(C_1)$	$\langle d_w^5\rangle/\langle d_w^3\rangle$	ε	$-\Delta P_1^*$	K (KDarcy)
10 ppi	0.37	5	0.8	34.1	81.8
15 ppi	0.41	3	0.89	46	45.3
20 ppi	0.36	2.1	0.82	39.3	30.2
30 ppi	0.36	1.6	0.88	38.4	24.9
40 ppi	0.33	0.78	0.86	27	15.8
50 ppi	0.31	0.55	0.88	23.9	11.9
−2.7 + 2 mm	0.39	1.22	0.79	39.6	18.1
−4 + 2.7 mm	0.37	2.01	0.8	38.7	29.6
−6.3 + 4 mm	0.29	8.72	0.85	31.1	131.5

done for a unit cell belonging to a packed bed filter, which permeability has been reported before.[10] The numerically and analytically computed ΔP_1^* values, for a packed bed of glass spheres, did not differ by more than 10 pct.[10]

Table V presents, for different filters, the values of the parameter involved in the calculation of the specific permeability according to Eq. [31]. From the table, it can be seen that the specific permeability varies directly with the ratio of fifth-to-third momenta of the window size distribution. Although porosity, dimensionless pressure drop, and $G(C_1)$ have an effect on permeability, no simple relationships can be observed from these data. Figure 11 presents calculated values of the dimensionless specific permeability, $K^* = K/d_c^2$, as a function of d_w/d_c. The plots correspond to porous structures with two window size distributions, narrow and wide, but the same average window diameter. The figure also includes the variation of the calculated porosity with the window-to-cell diameter ratio, for a pore structure with a coordination number of six. It can be seen that the plots for K^* and ε have a similar shape, but the dimensionless permeability shows a stronger dependence with d_w/d_c, specially for larger values. Such a strong dependence of K^* is a result of the effect that the constriction window has on the cell pressure drop, as seen in Figure 10(b). Figure 11 points out that the permeability is a function of the window size distribution; a narrow distribution leads to lower values of specific permeability. This result highlights the importance of controlling the structure of the filter precursor, polyurethane foam, or pore former particles in tailoring permeabilities. Haring and Greenkorn[25] found similar results about the effect of the radius distribution of pores on the permeability of packed beds. The window diameter distribution also affects the priming head of filters.[8,25]

Figure 12 shows a comparison between predicted and experimentally determined specific permeabilities. It can be seen that the permeability of both foam and CEFILPB filters are well described by the model. The permeability of CEFILPB filters were computed according to the following equation:

$$K = G(C_1)H(\alpha)\frac{\langle d_w^5\rangle\ \varepsilon_{ef}}{\langle d_w^3\rangle(-\Delta P_1^*)} \qquad [35]$$

where the effective porosity, $\varepsilon_{ef} = \varepsilon - \varepsilon_c$, has replaced

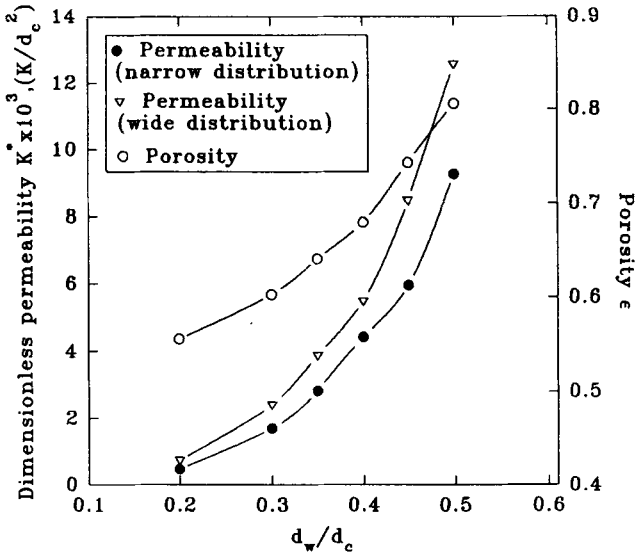

Fig. 11—Plots showing computed dimensionless specific permeability and porosity as a function of d_w/d_c. The permeability plots correspond to porous structures with narrow and wide window diameter distributions.

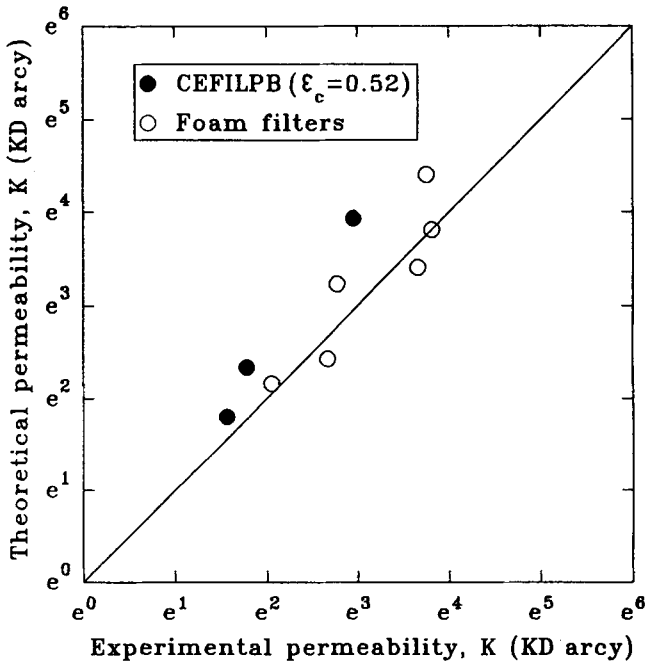

Fig. 12—Predicted *vs* experimentally determined specific permeabilities of foam and CEFILPB filters.

the porosity, ε, appearing in Eq. [31]. The effective porosity accounts for the fact that in filters of lost packed bed, there is a critical porosity, ε_c, obtained when the pore former spheres are just touching at one point; *i.e.*, the resulting pores are not connected. The critical porosity value corresponds to the ordinate intercept of the curves in Figure 5. For a coordination number of six, the critical porosity is 0.52. It should be noted that the foam filters do not require such a correction since their fabrication method is completely dissimilar from the CEFILPB's. A ceramic foam filter is an open filamentary net that will keep the pore connection independently

of the actual porosity. For this filter, no critical porosity is expected as long as this filamentary structure is not blocked by an excess of ceramic paste. Sane *et al.*[20] reported experimentally determined critical porosities for foam and pore former filters, ranging from 0.62 to 0.82; however, the authors do not elaborate on the nature of ε_c.

The results in Figure 12 give an indirect validation of the computed laminar fluid flow field in porous media used for molten metal filtration. Additional work on this topic is being focused in the calculation of particle trajectories and filtration efficiencies under pressure drop conditions encountered in actual filtration practices.

V. CONCLUSIONS

A general mathematical model has been developed to represent the fluid flow in ceramic foam filters used for molten metal filtration. The model is based on the analysis of creeping Newtonian fluid motion through a unit cell, geometric model, which resembles the pore structure of ceramic foam and pore former filters. The good agreement between experimental and computed permeabilities showed that the unit cell model approximates very well the effect of filter structure on the flow conditions inside the filter. The validity of the model is supported by the fact that permeabilities have been calculated from directly measured structural parameters; *i.e.*, there is no need to include any fitting parameters such as tortuosity nor connectivity. It was found that the permeability of the pore former filters depends on the porosity difference $\varepsilon - \varepsilon_c$ rather than on the porosity ε. This behavior reflects the influence of the fabrication method on the porosities that can be achieved, while maintaining interconnection between the pores. It was found that foam and CEFILPB filters have a coordination number of six. A critical porosity value of 0.52, for CEFILPB filters, was determined based on the rigid sphere model of a cubic lattice. The results indicate that the specific permeability is strongly dependent on the window size distribution. A close control of porosity and pore dimensions would allow one to tailor filter permeability values that respond to specific conditions.

The intended applications of the geometric and fluid flow models developed in this work are in the study of inclusion trajectories and the evaluation of filtration efficiencies as a function of structural parameters. This work will appear in a later publication.

APPENDIX

Relationship between the Distance x_0 and the Window Diameter d_w

From Figure 13 and using the Pitagoras' theorem, we have

$$(d_c/2)^2 = (d_w/2)^2 + x_0^2 \qquad [A1]$$

and recalling the definition for C_1, the distance between the centers of two adjacent pores is expressed by

$$2x_0 = d_w(C_1^2 - 1)^{1/2} \qquad [4]$$

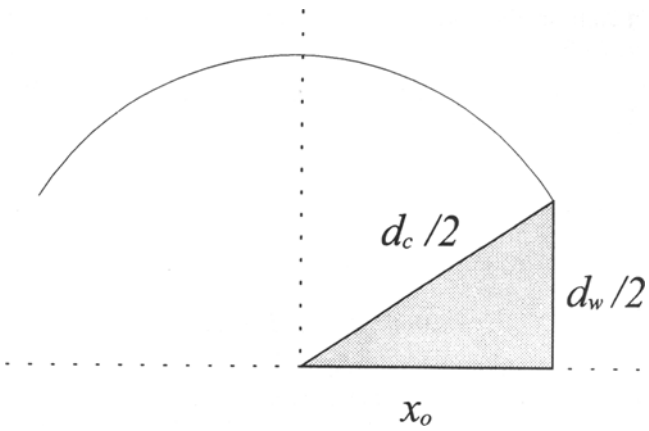

Fig. 13—Sketch of the section of a half-pore showing the relationship between d_c, d_w, and x_0.

Mean Volume of Unit Cells $\langle V_{UC} \rangle$

The volume of a unit cell is determined from the revolution solid formulae:

$$V_{UC} = \int_0^{2x_0} \pi r_s^2 d \qquad [A2]$$

where the radial distance, from the pore axis to the wall surface, r_s, is given by the Pitagoras' theorem (Figure 14) as follows:

$$r_c^2 = r_s^2 + (x - x_0)^2 \qquad [A3]$$

Combining Eqs. [A2] and [A3] and integrating, results in

$$V_{UC} = \pi[2r_c^2 x_0 - 2/3x_0^3] \qquad [A4]$$

and substitution of Eq. [3] in Eq. [A4] leads to

$$V_{UC} = \frac{\pi}{8}\left[2C_1^2(C_1^2 - 1)^{1/2} - \frac{2}{3}(C_1^2 - 1)^{3/2}\right]d_w^3 \qquad [A5]$$

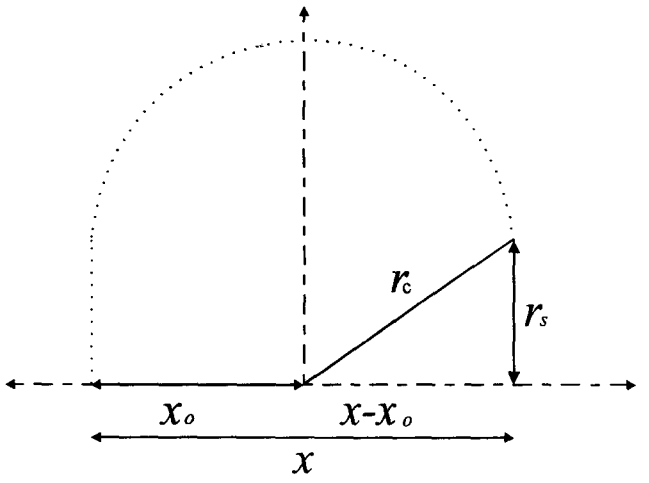

Fig. 14—Sketch of a section of a pore showing the relationship between r_c, r_s, x, and x_0.

therefore, the corresponding mean volume cell is given by

$$\langle V_{UC} \rangle = F(C_1)\langle d_w^3 \rangle \quad [28]$$

where,

$$F(C_1) = \frac{\pi}{8}\left[2C_1^2(C_1^2 - 1)^{1/2} - \frac{2}{3}(C_1^2 - 1)^{3/2}\right] \quad [30]$$

LIST OF SYMBOLS

a_1	laminar coefficient (Eq. [1])
a_2	turbulent coefficient (Eq. [1])
A	cross-sectional area of a pore at a given x-position, total cross-sectional area of the filter
A, B	Cartesian axes with origin located at the pore center
A_w	window cross-sectional area
C_1	ratio of cell-to-window diameters
d_c	randomly distributed cell diameter (mm)
$d_{c,max}$	maximum limit for the random diameter of a cell (mm)
$d_{c,min}$	minimum limit for the random diameter of a cell (mm)
d_w	randomly distributed window diameter (mm)
$\langle d_w^3 \rangle$	third momentum of the window diameter distribution (mm^3, Eq. [28])
$\langle d_w^5 \rangle$	fifth momentum of the window diameter distribution (mm^5, Eq. [25])
$E(d_w, \theta, \phi)$	joint probability density function of the random variables d_w, θ, and ϕ
f_{d_w}	fractional frequency of windows having a diameter d_w
$\mathbf{g}$	gravity acceleration vector
$F(C_1)$	geometric function defined by Eq. [29]
$G(C_1)$	geometric function defined by Eq. [32]
$H(\alpha)$	coordination number function (Eq. [33])
K	specific permeability (1 K Darcy = 10^{-5} cm^2)
L	side length of a cubic unit lattice
m_i	mass concentration of inclusions in the metal flow at the filter inlet
m_0	mass concentration of inclusions at the filter outlet
m_X	momentum of the fluid, in a pore, in the direction of the main flow (Eq. [13])
M_X	momentum of the fluid, in the whole filter, in the direction of the main flow (Eq. [10])
N	coordination number of a pore
N_p	number of pores per unit volume of filter (Eq. [26])
N_{Re}	Reynolds number
p	local pressure
P_1, P_2	pressures at the inlet and at the outlet of the filter, respectively
∇p	local pressure gradient
$\lvert\nabla P\rvert$	magnitude of the macroscopic pressure gradient (KPa/m) defined as the ratio $(P_1 - P_2)/\delta$
ΔP_1^*	dimensionless pressure drop in a unit cell, at Reynolds number equal to one (Eq. [20])
ΔP_{UC}	pressure drop through a unit cell, Eq. [7]
ΔP_{UC}^*	dimensionless pressure drop through a unit cell, Eq. [19]
q_{UC}	voluminic flow rate, in a cell, in the direction of the main flow, Eq. [15]
Q	voluminic flow rate through the whole filter, cm^3/s
Q_{UC}	voluminic flow rate through a cell, Eq. [18]
r_c	radius of a pore
r_s	radial distance from the axis of a pore to its wall
R_v^k	local value of the v-variable (pressure or velocity) in the k-iteration
$\mathbf{u}$	local fluid velocity
u_s	fluid superficial velocity
u_x	fluid velocity component in the direction of the pore axis
$[u_x]_X$	projection of u_x in the direction of the main flow
$\langle u_X \rangle$	mean fluid velocity, within the filter, in the direction of the main flow
u_w	mean velocity of the fluid at a window
V_m	total volume of the filter
V_{UC}	volume of a unit cell (Eq. [A6])
$\langle V_{UC} \rangle$	mean volume of the unit cells (Eq. [27])
V_s	volume of the spheres contained effectively in a unit lattice
V_t	total volume of a unit lattice
x, y	body-fitted coordinate axes located in a pore
x	axis of a pore; position along such an axis
X	axis in the direction of the main flow
x_0	distance from the center of a pore to the center of its window
α	limit value for θ under which axisymmetrical flow occurs
δ	filter thickness
∇	Nabla operator
ε	filter porosity
ε_c	filter critical porosity
ε_{ef}	filter effective porosity
ϕ	randomly distributed azimuthal angle
μ	fluid dynamic viscosity (Kg/μm s)
ν	fluid kinematic viscosity (μm^2/s)
θ	randomly distributed angle formed between the pore axis and the main flow direction
ρ	fluid density (Kg/μm^3)

ACKNOWLEDGMENTS

The authors are grateful to the Mexican Council of Science and Technology (CONACyT) for support of this work. The authors express their gratitude to Dr. Arturo Palacio for his useful advice in using the PHOENICS code.

REFERENCES

1. L.S. Aubrey and J.E. Dore: *Proc. 122nd TMS Annual Meeting*, Denver, CO, TMS, Warrendale, PA, 1993, pp. 1009-20.
2. W.H. Sutton, J.C. Palmer, and J.C. Morris: *AFS Trans.*, 1985, vol. 51, pp. 339-46.
3. L.S. Aubrey: *Foundry Trade J. Int.*, 1988, June, pp. 37-42.
4. L.S. Aubrey, J.W. Brockmeyer, and M.A. Mahuar: *Proc. 5th Int. Iron Steel Congress*, Iron and Steel Society, Washington, DC, 1986, vol. 69, pp. 977-91.
5. T. Komai, H. Takeuchi, Y. Nuri, and I. Sawada: *Proc. 5th Int. Iron Steel Congress*, Iron and Steel Society, Washington, DC, 1986, vol. 69, pp. 951-55.
6. R.W. Gairing and M. Cummings: *Iron Steel Maker*, 1993, vol. 20 (3), pp. 55-58.
7. D. Apelian, R. Mutharasan, C.A. Romanowski, R.E. Miller, and C.E. Eckert: *Proc. 111th TMS Annual Meeting*, Light Metals, Dallas, TX, 1982, pp. 935-68.
8. A.H. Castillejos-E., F.A. Acosta-G., and J.M. Almanza-R: *Proc. 121st TMS Annual Meeting*, San Diego, CA, TMS, Warrendale, PA, 1992, pp. 1113-22.
9. L.J. Heaslip, J.D. Dorricott, and P.J. Hoagland: *The Examination of Linear Cell Filter/Flow Modifiers for Improved Casting Quality through Enhanced Laminar Flow*, Technical Information, Premier Refractories Canada.
10. A.C. Payatakes, C. Tien, and R.M. Turian: *AICHE J.*, 1973, vol. 19 (1), pp. 58-76.
11. A.C. Payatakes, C. Tien, and R.M. Turian: *AICHE J.*, 1974, vol. 20 (5), pp. 889-905.
12. A.C. Payatakes and M. Neira: *AICHE J.*, 1977, vol. 23 (6), pp. 922-30.
13. C. Tian and R.I.L. Guthrie: *Proc. 122nd TMS Annual Meeting*, Denver, CO, TMS, Warrendale, PA, 1993, pp. 1003-07.
14. L.J. Gauckler, M.M. Waeber, C. Conti, and M. Jacob-Dulière: *Proc. 114th TMS Annual Meeting*, New York, NY, TMS, Warrendale, PA, 1985, pp. 1261-83.
15. T.A. Engh, B. Rasch, and E. Bathen: *Proc. 115th TMS Annual Meeting*, Light Metals, New Orleans, LA, TMS, Warrendale, PA, 1986, pp. 829-36.
16. F. Frisvold, T.A. Engh, S.T. Johansen, and T. Pedersen: *Proc. 121st TMS Annual Meeting*, Light Metals, San Diego, CA, TMS, Warrendale, PA, 1992, pp. 1125-32.
17. S.T. Johansen and N.M. Anderson: *Proc. EPD Congress 1990*, D.R. Gaskell, ed., TMS, Warrendale, PA, 1990, pp. 441-51.
18. J.M. Almanza-R.: B.Sc. Thesis, Instituto Tecnológico de Saltillo, Saltillo, Coah., México, Apr. 1990.
19. A.H. Castillejos-E., M. Méndez-N., F.A. Acosta-G., and J.M. Almanza-R.: Patent pending, Mexico, Registration no. 923671, SECOFI No. 5340, June 1992.
20. A.Y. Sane, D.J. Eichenmiller, and A.W. Gee: *Proc. 120th TMS Annual Meeting*, Orlando, FL, TMS, Warrendale, PA, 1991, pp. 1139-50.
21. W.E. Hollar, S.J. Lacki, H.G. Martin, and D.V. Neff: *Proc. 120th TMS Annual Meeting*, Orlando, FL, TMS, Warrendale, PA, 1991, pp. 1151-57.
22. A.Y. Sane, A.W. Gee, and D.J. Eichenmiller: U.S. Patent No. 5,028,036, July 2, 1991.
23. E.E. Underwood: *Quantitative Microscopy*, R.T. DeHoff and F.N. Rhines, eds., McGraw-Hill Book Co., New York, NY, 1974, pp. 149-99.
24. G.H. Geiger and D.R. Poirier: *Transport Phenomena in Metallurgy*, Addison-Wesley Publishing Co., Reading, MA, 1973, p. 94.
25. R.E. Haring and R.A. Greenkorn: *AICHE J.*, 1970, vol. 16 (3), pp. 477-83.